Extended Drude Model for Intraband-Transition-Induced Optical Nonlinearity

Heng Wang,[1] Kang Du,[1] Chuhao Jiang,[1] Zhiqiang Yang,[1] Lixia Ren,[1] Wending Zhang,[1,*] Soo Jin Chua,[1,2,3] and Ting Mei[1,†]

[1] *MOE Key Laboratory of Material Physics and Chemistry under Extraordinary Conditions, and Shaanxi Key Laboratory of Optical Information Technology, School of Science, Northwestern Polytechnical University, Xi'an 710072, China*

[2] *Department of Electrical and Computer Engineering, National University of Singapore, 4 Engineering Drive 3, Singapore 117583*

[3] *LEES Program, Singapore-MIT Alliance for Research & Technology (SMART), 1 CREATE Way, #10-01 CREATE Tower, Singapore 138602*

(Received 31 August 2018; revised manuscript received 4 March 2019; published 26 June 2019)

No existing model has completely explained the physics of the optical nonlinearity for epsilon-near-zero materials, which have recently emerged as candidates for design and fabrication of active nanophotonic devices. We propose to extend the Drude model by adopting a weighted electron effective mass, which takes into account the electron distribution in the nonparabolic conduction band. The extended Drude model is able to interpret the cause of the nonlinearity and provide a functional relationship between the refractive index and wavelength. Both the band nonparabolicity and the temperature-dependent mobility are responsible for the intraband-transition-induced optical nonlinearity. The spectrally resolved nonlinear refractive index and nonlinear susceptibilities are obtained from this model. The results can be applied to other transparent conducting oxides and will help in the design and modeling of spectral responses of nonlinear plasmonic devices.

DOI: 10.1103/PhysRevApplied.11.064062

I. INTRODUCTION

In recent years, the growing interest in nonlinear all-optical active nanophotonic devices has led to the development of high-speed, low-power, and large modulation depth switching devices [1–4]. The optical nonlinearities of materials play a crucial role in all-optical active nanophotonic devices [5]. All-optical controls at different wavelengths using a variety of plasmonic materials have been reported [5,6].

Large optical nonlinearities of the transparent conducting oxides (TCOs) [7,8], such as indium tin oxide (ITO) [9] and aluminum-doped zinc oxide (AZO) [10,11], were discovered at their epsilon-near-zero (ENZ) wavelengths. The unity order of refractive index changes of TCOs at ENZ wavelengths have attracted researchers' attention to the study of ENZ modes [12,13] and their strong coupling with plasmonic nanostructures [14–19]. A number of nanostructured all-optical active devices have been studied and exhibit advantages such as high modulation depth, ultrafast modulation speed, and low-power operation [17,20–22]. As the plasmonic materials with large optical nonlinearities at ENZ wavelengths [5,23], TCOs have become material platforms for integrated devices and metasurfaces [23,24].

The knowledge of Kerr-like optical nonlinearities of these materials is vital for designing the nanostructures as the nonlinearities vary greatly in the ENZ region [9]. Optical nonlinearities were experimentally investigated with experimental data presented at several discrete wavelengths [9,25], but this knowledge might not be sufficient for calculating nonlinear responses of nanostructures over a spectral region. Therefore, we need a general formalism to fill the gap between theory and experiment, which is able to provide the optical nonlinearities of TCOs over a spectral range.

The basis for calculating the change in permittivity is through the Drude model. One has to take into account the fact that the plasma frequency (ω_p) and the damping factor (γ) under intraband pumping are functions of the electron temperature (T_e) and the Fermi level (E_F). However, several authors have not considered the interdependence of ω_p, γ, m^* (electron effective mass), μ (electron mobility), E_F, and T_e. Guo *et al.* considered the relationship of ω_p on E_F, and T_e through the linearized collisionless Boltzmann equation [26] taking m^* and γ as constants [26,27]. Lyer *et al.* considered only the dependence of m^* on T_e through Hall measurement [21], leaving the dependence on unexplored E_F. Kim *et al.* extracted

*zhangwd@nwpu.edu.cn
†ting.mei@ieee.org

the values of m^* and μ induced by intraband transition from the pump-probe transmission spectra of nanocavities [22]. However, the relationship between T_e and m^* has not been proposed. In our formulation, ω_p and γ are measured through a pump-probe experiment and m^*, E_F, and T_e are related to one another through the conservation of electron concentration in intraband transitions when taking into account the nonparabolicity of the conduction band. The spectrally resolved nonlinear refractive index and nonlinear susceptibilities are obtained from this extended Drude model. At the same time, we are able to obtain the relaxation time of the excited carriers and deduce that the nonlinearity originates from both band nonparabolicity and temperature-dependent electron mobility.

II. MODEL

The relative permittivity of TCOs in the near-infrared (NIR) region is well described by the Drude model in the low optical intensity regime [6,7,28]

$$\varepsilon_r(\omega) = \varepsilon_\infty - \frac{\omega_p^2}{\omega^2 + i\gamma\omega}, \tag{1}$$

and

$$\omega_p^2 = \frac{Ne^2}{\varepsilon_0 m^*}, \quad \gamma = \frac{e}{m^*\mu}, \tag{2}$$

where ε_∞ is the high-frequency permittivity, ω is the optical angular frequency, N is the electron density, e is the electron charge, and ε_0 is the vacuum permittivity.

The Drude model treats the electron effective mass for all electrons in the free electron gas as identical. However, in materials with a nonparabolic electron band, the electron effective mass depends on energy [7], such that the conventional Drude model is no longer applicable for a collection of electrons with different energies. Therefore, the electron effective mass needs to be weighted to satisfy the intraband transition situation when considering optical nonlinearity if one is to retain the Drude model. The effective mass is derived as follows.

In the first-order nonparabolic approximation, the *E–k*relationship of ITO is expressed as [7,26,29]

$$\frac{\hbar^2 k^2}{2m_0^*} = E + CE^2, \tag{3}$$

where E is the electron energy referenced to the conduction band minimum, k is the wavevector, $\hbar$ is the reduced Planck constant, m_0^* is the electron effective mass at the conduction band minimum, and C is the first-order nonparabolicity factor. The electron density is derived as (see Appendix A)

$$N = \frac{1}{2\pi^2}\left(\frac{2m_0^*}{\hbar^2}\right)^{3/2}\int_0^\infty f_0(E + CE^2)^{1/2}(1 + 2CE)dE, \tag{4}$$

where $f_0 = \{\exp[(E - E_F)/(k_B T_e)] + 1\}^{-1}$ is the Fermi-Dirac distribution with E_F, T_e, and the Boltzmann constant k_B. N is conserved under intraband transition. For a given N, the E_F~T_e relation can be obtained using Eq. (4). With the presence of a large number of electrons at different energies, the electron effective mass to be used in the Drude model should be a statistically averaged value taking their distribution in energies into account, and is expressed in the following integration form (see Appendix A)

$$\frac{1}{m^*} = \frac{1}{2\pi^2 m_0^* N}\left(\frac{2m_0^*}{\hbar^2}\right)^{3/2}\int_0^\infty f_0(E + CE^2)^{1/2}dE. \tag{5}$$

The electron effective mass defined above could accurately predict the temperature-dependent free electron effective mass. With m^* defined above, ω_p and γ in Eq. (2) are thus defined, where the calculation of μ will be shown in the next section.

III. RESULTS AND DISCUSSION

We used ITO (supplier: Suzhou Research Materials Microtech Co., Ltd.) as the TCO to verify the model. The band gap of ITO is 3.5 eV, and the pump at the ENZ wavelength causes the intraband transition. The sample under test is a commercially available ITO film, with a thickness of 220 ± 10 nm, deposited on a 1.1-mm-thick flat glass substrate. The sheet resistance of the ITO film is 6 Ω/square. The high-frequency permittivity for ITO is $\varepsilon_\infty = 3.404$, similar to that in a previous report [30], and the first-order nonparabolicity factor is $C = 0.4191$ eV^{-1} [31]. In our work, $N = 1.5 \times 10^{21}$cm^{-3} is obtained by Hall measurement (see Supplemental Material) [32].

A femtosecond-pump-continuum-probe [33] experimental setup (Fig. 1) is adopted in this work to measure the transmittance $T(\omega)$ and reflectance $R(\omega)$ spectra from which the values of m^* and μ are extracted. The femtosecond laser operating at a wavelength of 1250 nm, a pulse width of 50 fs, and a repetition rate of 1 kHz is split into two beams. The pump beam is delayed and then focused on the sample by a lens at an incidence angle of 60° with p polarization, causing the maximum optical nonlinear response of ITO [9]. The probe beam is focused on a 5-mm-thick sapphire plate to generate a continuum beam [34] in the spectral range of 1000–1650 nm, which is subsequently attenuated and focused by a lens on the sample at normal incidence. The short axial length of the elliptical spot of the pump beam on the sample is about 500 μm, and

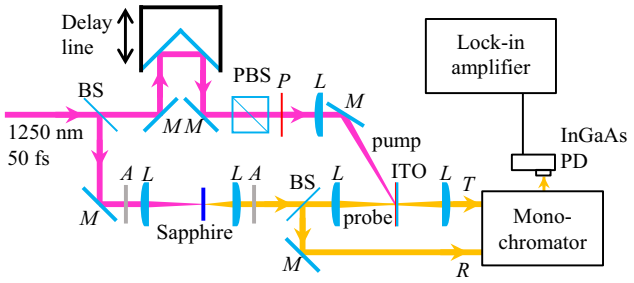

FIG. 1. Experimental setup of optical pump-continuum probe. M = mirror, L = lens, A = attenuator, BS = beam splitter, PBS = polarization beam splitter, P = polarizer, T = transmitted probe beam, R = reflected probe beam, PD = photodiode.

the diameter of the probe focal spot is about 50 μm. Such a geometric effect of oblique incidence brings an approximately 144 fs cross-correlation broadening of transient responses. Apart from this, the imperfect Gaussian shape with side lobes of the pulse may also broaden the rising and falling edges of pulse responses. The pump intensity (I_p) is tuned in the range of 0–140 GW/cm^2, while the probe intensity is reduced to lower than 1 GW/cm^2 to avoid probe-induced nonlinearity. In order to improve accuracy, both the transmittance and reflectance spectra of the probe beam are measured for extracting the Drude parameters ω_p and γ [35]. The Drude model and the transfer matrix method [36] are applied in the Levenberg-Marquardt optimization algorithm [37,38] to extract ω_p and γ from $T(\omega)$ and $R(\omega)$. Using Eq. (2), m^* and μ can be calculated.

Under zero pumping, the measured and fitted transmittance and reflectance spectra are shown in Fig. 2(a), which are in excellent agreement with published results [26]. The repeatability errors of ω_p and γ are less than 0.05 eV, while the 95% confidence bounds for fitting is less than 0.005 eV. The calculated permittivity spectrum using ω_p and γ is shown in Fig. 2(b), providing Re$\{\varepsilon_r\} = 0$ with a wavelength of 1214 nm. With the value of ω_p, m^* can be calculated from Eq. (2).

The next step is to calculate the value of m_0^*. At zero pumping, T_e is room temperature (300 K), thus

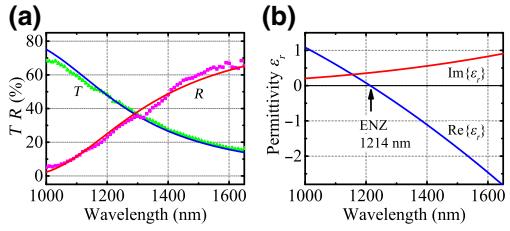

FIG. 2. (a) Measured transmittance and reflectance spectra in the case of zero pumping and the fitted curve. (b) Calculated real and imaginary parts of permittivity of the ITO film. The Re$\{\varepsilon_r\} = 0$ wavelength occurs at 1214 nm.

$E_F = 0.8793$ eV can be numerically calculated from Eq. (4). Using the value of m^* obtained at room temperature, and with E_F and T_e at room temperature, the value of m_0^* is found from Eq. (5) to be $m_0^*/m_e = 0.3964$, where m_e is the electron rest mass.

The dependence of ω_p and γ on pump intensity (I_p) are studied for the peak nonlinear response. The measured transmittance and reflectance spectra at zero delay shown in Figs. 3(a) and 3(b) exhibit a saturation trend with increasing I_p. Such a trend is better illustrated by the plots of the calculated ω_p and γ vs I_p in Fig. 3(c). The saturation trend of $\omega_p(I_p)$ is consistent with that reported previously in which the $\omega_p(I_p)$ is extracted from the plasmon resonance spectroscopy of ITO nanorod arrays [26].

As governed by Eq. (5), m^* increases with increasing T_e for positive C, as seen in the plot of m^* vs T_e in Fig. 3(d). The mobility decreases with increasing T_e as seen in Fig. 3(d), and the curve fitting provides $\mu = 18.3 - 2.13 \times 10^{-5} T_e^{1.53}$ (solid line) in which the exponential index 1.53 is close to 3/2, indicating that ionized impurity scattering is the dominant scattering

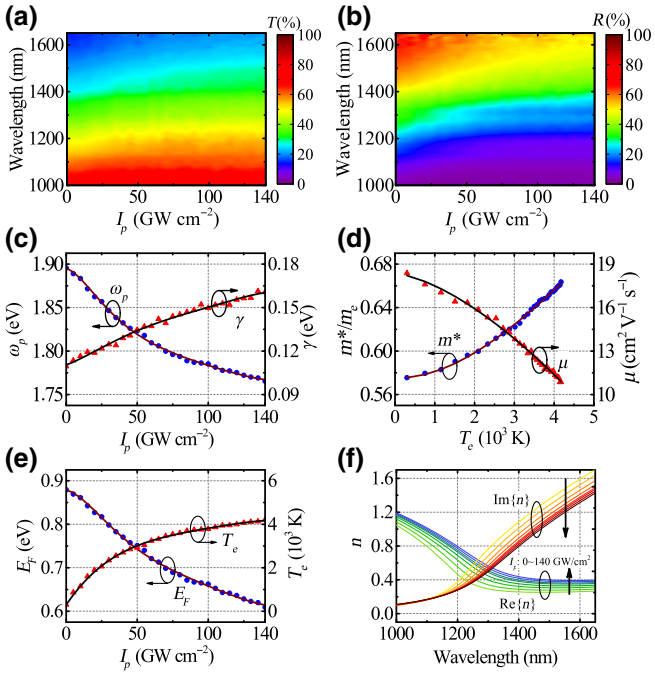

FIG. 3. Measured I_p-dependent transmittance spectra (a) and reflectance spectra (b). (c)–(e) Calculated I_p-dependent responses of ω_p and γ, m^* and μ, and E_F and T_e. The solid lines are theoretical curves: the $\mu \sim T_e$ relation is given by $\mu = 18.3 - 2.13 \times 10^{-5} T_e^{1.53}$, $T_e \sim I_p$ is the polynomial fitting, $E_F \sim I_p$ is calculated by substituting $T_e \sim I_p$ in Eq. (4), $m^* \sim T_e$ is calculated from Eqs. (4) and (5), and $\omega_p \sim I_p$ and $\gamma \sim I_p$ are calculated from Eq. (2).The theoretical curves are in perfect agreement with the experiment. (f) Real and imaginary parts of the complex refractive index calculated from ω_p and γ in Fig. 3(c) from 0 to 140 GW/cm^2 with a 20 GW/cm^2 step.

mechanism [7,39]. In many cases, especially those using the two-temperature model, the relations between Drude parameters and T_e are useful, and they are plotted in Fig. 7 (Appendix B).

The saturation trend of the $T_e \sim I_p$ relation illustrated in Fig. 3(e) shows that the electron heat capacity increases as the electron temperature rises, consistent with the previously reported work [26] and fitted by a polynomial function (solid line). The saturation of T_e with I_p leads to the saturation of m^*, μ, ω_p, and γ in their relations with I_p.

The I_p-dependent real and imaginary parts of the complex refractive index [Fig. 3(f)] are calculated using Eq. (1) with the above obtained values of $\omega_p(I_p)$ and $\gamma(I_p)$. The I_p-dependent complex refractive index at the $\mathrm{Re}\{\varepsilon_r\} = 0$ wavelength is plotted in Fig. 4(a) and exhibits a saturation trend with increasing I_p. The relative permittivity in Eq. (1) can be rewritten in terms of m^* and μ as

$$\varepsilon_r = \varepsilon_\infty - \frac{Ne^2}{\varepsilon_0(m^*\omega^2 + ie\omega/\mu)}, \tag{6}$$

which is a function of the implicit variable T_e. In nonlinear optics, the relative permittivity is expressed in the form of

$$\varepsilon_r = 1 + \chi^{(1)}(\omega) + 6\chi^{(3)}(\omega : \omega', -\omega', \omega)|E_p(\omega')|^2 + 20\chi^{(5)}(\omega : \omega', -\omega', \omega', -\omega', \omega)|E_p(\omega')|^4 + \cdots, \tag{7}$$

where E_p is the pumping electric field. Comparing Eqs. (6) and (7), it is clear that the origin of nonlinear susceptibilities is in the $m^* \sim I_p$ and $\mu \sim I_p$ relations. The spectrally resolved third- and fifth-order nonlinear susceptibilities are obtained by polynomial fitting the $\varepsilon_r \sim I_p$ curve at each wavelength and are shown in Figs. 4(c) and 4(d). The nonlinear susceptibilities at the $\mathrm{Re}\{\varepsilon_r\} = 0$ wavelength are in the same order of magnitude as those above, but are slightly smaller than the previously reported results [25]. The differences are mainly due to different pumping and ENZ wavelengths. Note that the nonlinear susceptibilities are monotonically varying at the ENZ wavelengths [Figs. 4(c) and 4(d)] where the $\mathrm{Re}\{\Delta n\}$ peak appears [Fig. 4(b)] due to the enhancement effect of ENZ on optical nonlinearity, that is, $\Delta n = \Delta\varepsilon/(2\sqrt{\varepsilon})$, and the continuity of the electric displacement field across the ITO-air interface [9]. The spectrally resolved nonlinear susceptibilities [$\chi^{(3)}$, $\chi^{(5)}$] shown in Figs. 4(c) and 4(d), which is the key result of this study, will help researchers in calculating the spectral responses of nonlinear all-optical active nanophotonic devices.

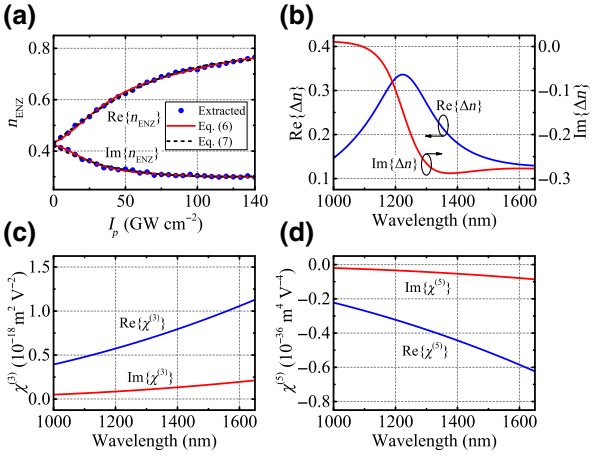

FIG. 4. (a) The I_p-dependent real and imaginary parts of the complex refractive index at $\mathrm{Re}\{\varepsilon_r\} = 0$ wavelength. The three sets of curves are the measured results and are calculated using the Drude model and the optical nonlinear model, respectively. (b) The real and imaginary parts of the refractive index change under 140 GW/cm^2 pumping with respect to zero pumping. Spectrally resolved real and imaginary parts of the third-order (c) and fifth-order (d) complex nonlinear susceptibility.

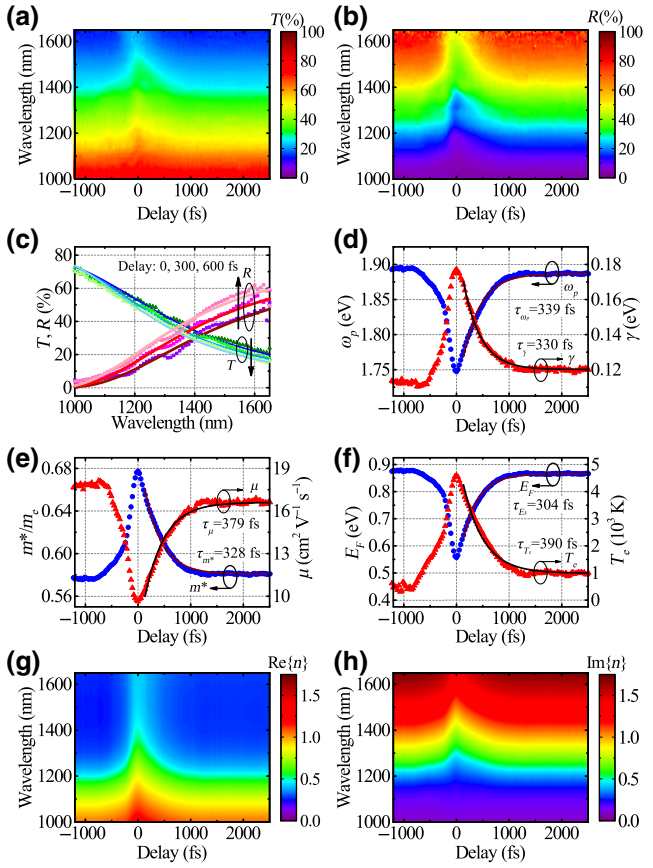

FIG. 5. Measured spectrally resolved transient transmittance (a) and reflectance (b) responses of the ITO film, and their slices and fitted curves (c) at 0, 300, and 600 fs, respectively. (d)–(f) Calculated transient responses of ω_p and γ, m^* and μ, and E_F and T_e, the falling edges of which are fitted by the exponential decay function $y(t) = y_0 + [y(I) - y_0]\exp(-t/\tau_y)$ (solid lines) and the relaxation times τ are shown. The transient real (g) and imaginary (h) parts of the refractive index of the ITO film are calculated using Eq. (1) with $\omega_p(t)$ and $\gamma(t)$ in (d).

The experiment for the transient nonlinear optical response is carried out with $I_p = 140$ GW/cm^2. As shown in Figs. 5(a) and 5(b), the transmittance and reflectance spectra of a series of pump-probe delays show delay-dependent variations. Figure 5(c) illustrates the transmittance and reflectance spectra and their fitting curves at 0, 300, and 600 fs. The Drude model is applicable in assumption of a quasiequilibrium process. Thus, the time-dependent Drude parameters, $\omega_p(t)$ and $\gamma(t)$, can be extracted by curve fitting the transmittance and reflectance spectra, then forming a transient response curve in Fig. 5(d). It can be seen that ω_p decreases while γ increases in value when the ITO film undergoes the femtosecond pump, and after that, they relax back to their original values with time. Their relaxation times are both on the order of hundreds of femtoseconds. By curve fitting the falling edges of $\omega_p(t)$ and $\gamma(t)$ using exponential functions, the relaxation times are determined as 339 and 330 fs, respectively.

When the pump pulse interacts with ITO, energy is transferred to electrons, resulting in a T_e rise [Fig. 5(f)] and redistribution of electrons, as described by the Fermi-Dirac distribution function. This leads to an increase in the value of m^* [Eq. (5) and Fig. 5(e)] and a decrease in the value of ω_p [Eq. (2) and Fig. 5(d)]. Immediately after the pumping is over, there is a relaxation process in which the energy is transferred from electrons to the lattice as heat and then dissipates. This dynamic process is usually described using the two-temperature model [9,40], and the extended Drude model, presented in this paper, interprets the consequent optical nonlinearity with the corresponding statistically averaged electronic parameters m^* and μ. Different pump beam configurations, that is, with different pulse energy and pulse width, will yield different results. As shown in Fig. 5(e), accompanying the decay of T_e, m^* and μ are relaxed at $\tau_{m^*} = 328$ fs and $\tau_\mu = 379$ fs, respectively.

The real and imaginary parts of the transient complex refractive index n of the ITO film can be calculated using Eq. (1) with $\omega_p(t)$ and $\gamma(t)$ presented in Fig. 5(d). As shown in Figs. 5(g) and 5(h), the Real (Imaginary) part of the refractive index experiences rising (falling) and recovery stages in unit order in hundreds of femtoseconds in the NIR range under ENZ pumping.

IV. CONCLUSION

Optical nonlinearity induced by intraband transition is studied from the electron response, which is measured by a femtosecond-pump-continuum-probe experiment. The extended Drude model adopts a weighted effective mass (m^*), which takes into account the electron redistribution in the nonparabolic conduction band during optical excitation. Through the study of intensity dependence and transient responses of the plasma frequency (ω_p) and the damping factor (γ), it is found that the nonlinearity originates from both the band nonparbolicity and the temperature-dependent electron mobility (μ). In the ITO sample studied, the dominant electron scattering mechanism is due to ionized impurity. During the relaxation process of the excited electrons, the relaxation times for m^* and μ are found to be 328 and 379 fs, and those of ω_p and γ are 339 and 330 fs, respectively. The nonlinear refractive indices and nonlinear susceptibilities are spectrally resolved in this study. The results can be applied to other TCOs and will help researchers in designing the spectral and transient responses of nonlinear all-optical active nanophotonic devices.

ACKNOWLEDGMENTS

We acknowledge the financial support from Natural Science Foundation of China (NSFC) (Grants No. 61675171 and No. 61675169), Shaanxi Provincial Key R&D program (Grant No. 2018KW-009), Fundamental Research Funds for the Central Universities (Grants No. 3102017HQZZ022 and No. 3102017zy021), and Seed Foundation of Innovation and Creation for Graduate Students in Northwestern Polytechnical University (Grant No. ZZ2018180).

APPENDIX A: EFFECTIVE MASS OF NONPARABOLIC CONDUCTION BAND

The E–k relation for a nonparabolic conduction band (Fig. 6a) is

$$\frac{\hbar^2 k^2}{2m_0^*} = E + CE^2. \tag{A1}$$

In an isotropic band, the total number of states, n_s, in a spherical region of the k space with a radius of k is

$$n_s = \frac{4}{3}\pi\left(\frac{k}{2\pi}\right)^3 = \frac{k^3}{3\pi^2}. \tag{A2}$$

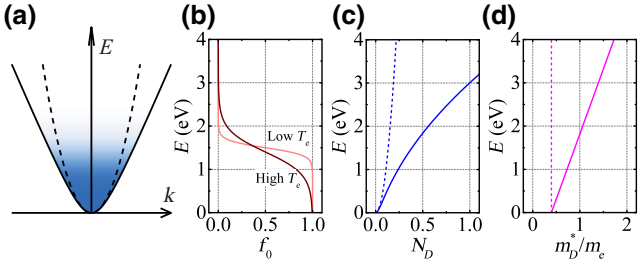

FIG. 6. (a) The $E - k$ relation. (b) Fermi-Dirac distribution for different electron temperatures. (c) Density of states. (d) Density of states effective mass. In (a, c, d), the dashed lines are the parabolic band and solid lines are the nonparabolic band.

Substituting Eq. (A1) obtains

$$n_s = \frac{1}{3\pi^2}\left(\frac{2m_0^*}{\hbar^2}\right)^{3/2}(E + CE^2)^{3/2}, \tag{A3}$$

and the density of states is (Fig. 6c) [7]

$$N_D = \frac{dn_s}{dE} = \frac{1}{2\pi^2}\left(\frac{2m_0^*}{\hbar^2}\right)^{3/2}(E + CE^2)^{1/2}(1 + 2CE). \tag{A4}$$

The distribution of electrons in the conduction band can be described by the Fermi-Dirac distribution (Fig. 6b)

$$f_0 = \frac{1}{\exp[(E - E_F)/(k_B T_e)] + 1}. \tag{A5}$$

The electron density N is

$$N = \int_0^\infty f_0 N_D dE. \tag{A6}$$

Substituting Eq. (A4) obtains

$$N = \frac{1}{2\pi^2}\left(\frac{2m_0^*}{\hbar^2}\right)^{3/2}\int_0^\infty f_0(E + CE^2)^{1/2}(1 + 2CE)dE, \tag{A7}$$

which is Eq. (4) in the main text and is the same as that previously reported [26]. For $C \to 0$, that is, a parabolic conduction band, the usual expression for electron density

$$N = \frac{1}{2\pi^2}\left(\frac{2m_0^*}{\hbar^2}\right)^{3/2}\int_0^\infty f_0 E^{1/2} dE, \tag{A8}$$

is recovered [41]. The momentum effective mass of electrons is

$$\frac{1}{m^*} = \frac{1}{p}\frac{dE}{dp}, \tag{A9}$$

and

$$\frac{1}{m^*} = \frac{1}{\hbar^2 k}\frac{dE}{dk}. \tag{A10}$$

Substituting Eq. (A1) obtains the density-of-states effective mass (Fig. 6d) [7,29]

$$m_D^* = m_0^*(1 + 2CE). \tag{A11}$$

The overall effective mass statistically averages the effective mass over the electron distribution in the conduction band by the integration form with weights of $f_0 N_D/N$

$$\frac{1}{m^*} = \frac{1}{N}\int_0^\infty \frac{f_0 N_D}{m_D^*} dE. \tag{A12}$$

Substituting Eqs. (A4) and (A11),

$$\frac{1}{m^*} = \frac{1}{2\pi^2 m_0^* N}\left(\frac{2m_0^*}{\hbar^2}\right)^{3/2}\int_0^\infty f_0(E + CE^2)^{1/2} dE, \tag{A13}$$

which is Eq. (5) in the main text. Equation (A13) is reduced to $m^* = m_0^*$ for $C \to 0$, that is a parabolic conduction band.

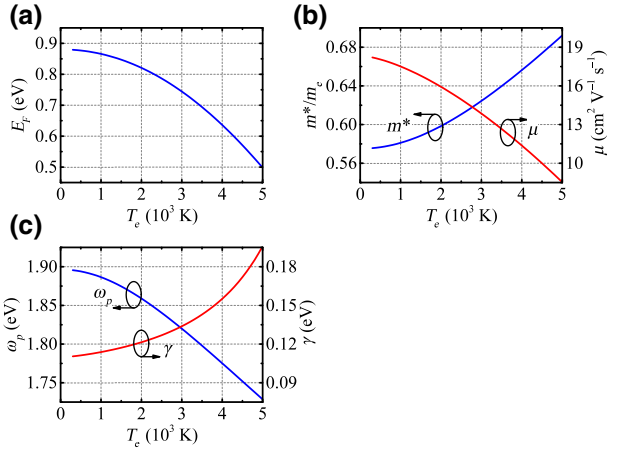

FIG. 7. Electron temperature-dependent (a) Fermi level, (b) electron total effective mass and mobility, and (c) plasma frequency and damping factor.

APPENDIX B: CALCULATION OF ELECTRON TEMPERATURE

Upon pumping at the ENZ wavelength, only intraband transition occurs and thus the electron density N is conserved. Using Eq. (A7) the $E_F \sim T_e$ relation [Fig. 7(a)] is numerically obtained [26,27]. The $m^* \sim T_e$ relation [Fig. 7(b)] is obtained by substituting the $E_F \sim T_e$ relation in Eq. (A13). The $\mu \sim T_e$ relation is the curve fitting ($\mu = 18.3 - 2.13 \times 10^{-5} T_e^{1.53}$) in the main text. The $\omega_p \sim T_e$ and $\gamma \sim T_e$ relations [Fig. 7(c)] are calculated from Eq. (2).

[1] D. A. Miller, Are optical transistors the logical next step?, Nat. Photonics **4**, 3 (2010).
[2] Z. Ma, Z. Li, K. Liu, C. Ye, and V. J. Sorger, Indium-tin-oxide for high-performance electro-optic modulation, Nanophotonics **4**, 198 (2015).

[3] S. Jahani and Z. Jacob, All-dielectric metamaterials, Nat. Nanotechnol. **11**, 23 (2016).

[4] Y. U. Lee, E. Garoni, H. Kita, K. Kamada, B. H. Woo, Y. C. Jun, S. M. Chae, H. J. Kim, K. J. Lee, and S. Yoon, Strong nonlinear optical response in the visible spectral range with epsilon-near-zero organic thin films, Adv. Opt. Mater. **6**, 1701400 (2018).

[5] V. Krasavin Alexey, P. Ginzburg, and V. Zayats Anatoly, Free-electron optical nonlinearities in plasmonic nanostructures: a review of the hydrodynamic description, Laser Photon. Rev. **12**, 1700082 (2017).

[6] G. V. Naik, V. M. Shalaev, and A. Boltasseva, Alternative plasmonic materials: beyond gold and silver, Adv. Mater. **25**, 3264 (2013).

[7] H. Hosono, D. Paine, and D. Ginley, *Handbook of Transparent Conductors* (Springer Science & Business Media, New York, 2010).

[8] J. Gao, K. Kempa, M. Giersig, E. Akinoglu, B. Han, and R. Li, Physics of transparent conductors, Adv. Phys. **65**, 553 (2016).

[9] M. Z. Alam, I. De Leon, and R. W. Boyd, Large optical nonlinearity of indium tin oxide in its epsilon-near-zero region, Science **352**, 795 (2016).

[10] N. Kinsey, C. DeVault, J. Kim, M. Ferrera, V. Shalaev, and A. Boltasseva, Epsilon-near-zero Al-doped ZnO for ultrafast switching at telecom wavelengths, Optica **2**, 616 (2015).

[11] L. Caspani, R. P. M. Kaipurath, M. Clerici, M. Ferrera, T. Roger, J. Kim, N. Kinsey, M. Pietrzyk, A. Di Falco, V. M. Shalaev, A. Boltasseva, and D. Faccio, Enhanced Nonlinear Refractive Index in ϵ-Near-Zero Materials, Phys. Rev. Lett. **116**, 233901 (2016).

[12] S. Vassant, A. Archambault, F. Marquier, F. Pardo, U. Gennser, A. Cavanna, J. L. Pelouard, and J. J. Greffet, Epsilon-Near-Zero Mode for Active Optoelectronic Devices, Phys. Rev. Lett. **109**, 237401 (2012).

[13] S. Campione, I. Brener, and F. Marquier, Theory of epsilon-near-zero modes in ultrathin films, Phys. Rev. B **91**, 121408 (2015).

[14] S. Campione, J. R. Wendt, G. A. Keeler, and T. S. Luk, Near-infrared strong coupling between metamaterials and epsilon-near-zero modes in degenerately doped semiconductor nanolayers, ACS Photonics **3**, 293 (2016).

[15] J. Kim, A. Dutta, G. V. Naik, A. J. Giles, F. J. Bezares, C. T. Ellis, J. G. Tischler, A. M. Mahmoud, H. Caglayan, O. J. Glembocki, A. V. Kildishev, J. D. Caldwell, A. Boltasseva, and N. Engheta, Role of epsilon-near-zero substrates in the optical response of plasmonic antennas, Optica **3**, 339 (2016).

[16] S. A. Schulz, A. A. Tahir, M. Z. Alam, J. Upham, I. De Leon, and R. W. Boyd, Optical response of dipole antennas on an epsilon-near-zero substrate, Phys. Rev. A **93**, 063846 (2016).

[17] M. Z. Alam, S. A. Schulz, J. Upham, I. De Leon, and R. W. Boyd, Large optical nonlinearity of nanoantennas coupled to an epsilon-near-zero material, Nat. Photonics **12**, 79 (2018).

[18] Y. C. Jun, J. Reno, T. Ribaudo, E. Shaner, J.-J. Greffet, S. Vassant, F. Marquier, M. Sinclair, and I. Brener, Epsilon-near-zero strong coupling in metamaterial-semiconductor hybrid structures, Nano Lett. **13**, 5391 (2013).

[19] K. Minn, A. Anopchenko, J. Yang, and H. W. H. Lee, Excitation of epsilon-near-zero resonance in ultra-thin indium tin oxide shell embedded nanostructured optical fiber, Sci. Rep. **8**, 2342 (2018).

[20] Q. Guo, Y. Cui, Y. Yao, Y. Ye, Y. Yang, X. Liu, S. Zhang, X. Liu, J. Qiu, and H. Hosono, A solution-processed ultrafast optical switch based on a nanostructured epsilon-near-zero medium, Adv. Mater. **29**, 1700754 (2017).

[21] P. P. Iyer, M. Pendharkar, C. J. Palmstrøm, and J. A. Schuller, Ultrawide thermal free-carrier tuning of dielectric antennas coupled to epsilon-near-zero substrates, Nat. Commun. **8**, 472 (2017).

[22] J. Kim, E. G. Carnemolla, C. DeVault, A. M. Shaltout, D. Faccio, V. M. Shalaev, A. V. Kildishev, M. Ferrera, and A. Boltasseva, Dynamic control of nanocavities with tunable metal oxides, Nano Lett. **18**, 740 (2018).

[23] N. X., H. X., C. S., and G. Q., Epsilon-near-zero photonics: a new platform for integrated devices, Adv. Opt. Mater. **6**, 1701292 (2018).

[24] M. Choudhury Sajid, D. Wang, K. Chaudhuri, C. DeVault, V. Kildishev Alexander, A. Boltasseva, and M. Shalaev Vladimir, Material platforms for optical metasurfaces, Nanophotonics **7**, 959 (2018).

[25] O. Reshef, E. Giese, M. Zahirul Alam, I. De Leon, J. Upham, and R. W. Boyd, Beyond the perturbative description of the nonlinear optical response of low-index materials, Opt. Lett. **42**, 3225 (2017).

[26] P. Guo, R. D. Schaller, J. B. Ketterson, and R. P. Chang, Ultrafast switching of tunable infrared plasmons in indium tin oxide nanorod arrays with large absolute amplitude, Nat. Photonics **10**, 267 (2016).

[27] B. T. Diroll, P. Guo, R. P. H. Chang, and R. D. Schaller, Large transient optical modulation of epsilon-near-zero colloidal nanocrystals, ACS Nano **10**, 10099 (2016).

[28] M. D. Losego, A. Y. Efremenko, C. L. Rhodes, M. G. Cerruti, S. Franzen, and J.-P. Maria, Conductive oxide thin films: Model systems for understanding and controlling surface plasmon resonance, J. Appl. Phys. **106**, 024903 (2009).

[29] T. Pisarkiewicz and A. Kolodziej, Nonparabolicity of the conduction band structure in degenerate tin dioxide, Phys. Status Solidi B **158**, K5 (1990).

[30] C. G. Granqvist and A. Hultåker, Transparent and conducting ITO films: new developments and applications, Thin Solid Films **411**, 1 (2002).

[31] X. Liu, J. Park, J.-H. Kang, H. Yuan, Y. Cui, H. Y. Hwang, and M. L. Brongersma, Quantification and impact of nonparabolicity of the conduction band of indium tin oxide on its plasmonic properties, Appl. Phys. Lett. **105**, 181117 (2014).

[32] See Supplementary Information at http://link.aps.org/supplemental/10.1103/PhysRevApplied.11.064062 for the Hall measurement results and the fitting goodness with different optical nonlinear susceptibility orders.

[33] R. W. Schoenlein, W. Z. Lin, E. P. Ippen, and J. G. Fujimoto, Femtosecond hot-carrier energy relaxation in GaAs, Appl. Phys. Lett. **51**, 1442 (1987).

[34] H. Nishioka, W. Odajima, K.-i. Ueda, and H. Takuma, Ultrabroadband flat continuum generation in multichannel propagation of terrawatt Ti:sapphire laser pulses, Opt. Lett. **20**, 2505 (1995).

[35] R. J. Mendelsberg, G. Garcia, and D. J. Milliron, Extracting reliable electronic properties from transmission spectra of indium tin oxide thin films and nanocrystal films by careful application of the Drude theory, J. Appl. Phys. **111**, 063515 (2012).

[36] C. C. Katsidis and D. I. Siapkas, General transfer-matrix method for optical multilayer systems with coherent, partially coherent, and incoherent interference, Appl. Opt. **41**, 3978 (2002).

[37] K. Levenberg, A method for the solution of certain nonlinear problems in least squares, Quart. Appl. Math. **2**, 436 (1944).

[38] D. W. Marquardt, An algorithm for least-squares estimation of nonlinear parameters, J. Soc. Ind. Appl. Math. **11**, 431 (1963).

[39] P. Y. Yu, M. Cardona, and L. J. Sham, *Fundamentals of Semiconductors: Physics and Materials Properties* (Zeitschrift Für Physikalische Chemie, New York, 2010).

[40] G. V. Hartland, Optical studies of dynamics in noble metal nanostructures, Chem. Rev. **111**, 3858 (2011).

[41] J. Singh, *Electronic and Optoelectronic Properties of Semiconductor Structures* (Cambridge University Press, New York, 2007).